ACS Catalysis

pubs.acs.org/acscatalysis Research Article

Room-Temperature CO Oxidative Coupling for Oxamide Production over Interfacial Au/ZnO Catalysts

Yanwei Cao,[⊥] Yao Peng,[⊥] Danyang Cheng,[⊥] Lin Chen, Maolin Wang, Cheng Shang, Lirong Zheng, Ding Ma,* Zhi-Pan Liu,* and Lin He*

Cite This: *ACS Catal.* 2023, 13, 735−743 Read Online

ACCESS | Metrics & More | Article Recommendations | Supporting Information

ABSTRACT: The conversion of carbon monoxide (CO) into high-value organic molecules has long been pursued by both industry and academia. One of the central challenges is to realize carbon−carbon coupling with high selectivity for CO insertion. We report here a highly selective Au/ZnO composite catalyst for one-step oxidative coupling of CO with secondary amines, producing oxamides. The reaction is >99% selective under ambient conditions, which exhibits a subtle change of catalyst activity over ∼120 h in a fixed-bed reactor. A combination of microscopic and spectroscopic studies (including X-ray photoemission spectroscopy, X-ray absorption spectroscopy, CO-Fourier transform infrared spectroscopy, and aberration-corrected high-angle annular dark-field scanning transmission electron microscopy) and machine learning reveal that the active site is the Au−ZnO interface with a Au nanocluster attached to the ZnO support *via* nonstoichiometric ZnO_x ($x > 1$) linkages. The reaction mechanism and key reaction intermediates were confirmed by density functional theory calculations and *in situ* diffused reflectance infrared Fourier transform spectroscopy signals. Our results open an avenue in heterogeneous catalysis to achieve the ambient-condition CO transformation by exploiting the interfacial synergistic effects.

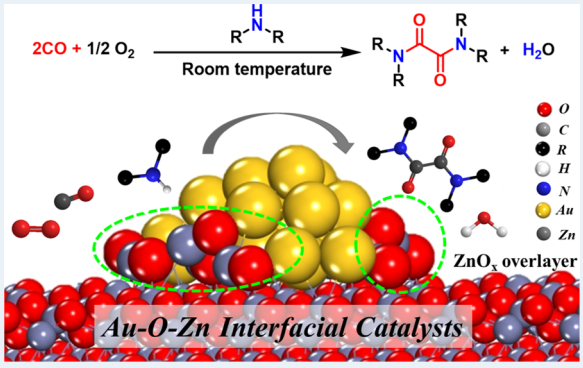

KEYWORDS: *gold, zinc oxide, interfacial catalysts, CO, oxidative coupling, oxamide*

1. INTRODUCTION

The selective conversion of CO into value-added chemicals under mild conditions is an appealing but challenging task in chemistry.[1,2] Due to the high barriers of CO activation, approaches to carbon−carbon coupling, for example, those using heterogeneous catalysis generally require relatively high temperatures, which disfavor selectivity.[2−10] In particular, oxidative conditions are generally prohibited as the carbon dioxide (CO_2) would dominate the reaction.[11−13] The current ambient-condition C−C coupling reactions rely primarily on electro- or photocatalysis or homogeneous catalysis.[14−18] For instance, Pd complex catalysts can catalyze CO oxidative coupling (also known as double carbonylation[19−21]) to oxamides at room temperature. However, such homogeneous catalysis usually involves sophisticated and expensive ligands and substantial amounts of corrosive iodine (5−50 mol % relative to substrate) to complete the catalytic cycle.[18,22−25]

As oxamides can serve as important feedstocks for the production of bulk chemicals, such as oxalic acid, oxalates, and ethylene glycol,[18,24,26−28] the development of heterogenous catalytic systems is highly desirable for many reasons, including the ease of continuous production and reusability of the catalyst and environmental compatibility. Recently reported encouraging progress showed that a Au/hydrotalcite (HT) catalyst can catalyze the CO oxidative coupling producing oxamides at relatively high temperatures of 110−150 °C.[29] As the mechanistic insights into this reaction are not available yet, it is the aim of this work to screen the reaction sites and develop better heterogeneous catalysts for CO oxidative coupling under ambient conditions.

Herein, we report a Au/ZnO nanocatalyst that has high selectivity (99%) and long-term stability for CO oxidative coupling with diverse secondary amines to produce oxamides at room temperature. By combining a series of experimental techniques and the latest large-scale machine learning atomic simulations,[30] we have shown that the interface between Au nanoparticles and nonstoichiometric ZnO_x complexes on ZnO is the active site for the low-temperature CO oxidative coupling. When amines are present, the catalyst switches from CO oxidation to CO oxidative coupling, and the reaction

Received: October 31, 2022
Revised: December 14, 2022
Published: December 23, 2022

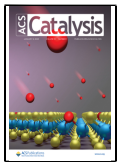

https://doi.org/10.1021/acscatal.2c05358
ACS Catal. 2023, 13, 735−743

is further boosted under rich O_2 conditions. This work opens a new vista

for ambient-temperature CO transformation with C−C bond formation by interfacial catalysis.

2. EXPERIMENTAL SECTION

2.1. Chemicals. $Zn(NO_3)_2{\cdot}6H_2O$ was obtained from Sino-Pharm Chemical Reagent Company. Na_2CO_3, $HAuCl_4{\cdot}3H_2O$, and morpholine were obtained from Adamas-β. Synthetic air and carbon monoxide (≥99.95%) were purchased in cylinders from Air Liquid. Other reagents were of analytical grade and used as purchased from Energy Chemical, Aladdin, and Macklin without purification.

2.2. Preparation of Zinc Oxide (ZnO). The ZnO supports were prepared by the precipitation method using sodium carbonate as a precipitant. An aqueous solution (200 mL) containing $Zn(NO_3)_2{\cdot}6H_2O$ (37.5 g) was stirred at room temperature, and the sodium carbonate solution (200 mL, 1.2 equiv) was slowly added to the zinc nitrate solution. The suspension was stirred for another 3 h and aged for 12 h at room temperature. Then, the precipitate was filtered and washed with deionized water five times until the pH of the washings reached pH 7. After being dried at 60 °C for 12 h in an oven, the precipitate was calcined in air at 500 °C (5 °C min^{-1}) for 2 h.

2.3. Preparation of Au/ZnO. Au/ZnO was prepared by a deposition−precipitation (DP) method. In a typical synthesis of 1 wt % Au/ZnO, ZnO (2 g) was added to deionized water (50 mL) containing the amount of $HAuCl_4{\cdot}3H_2O$ necessary to obtain a 1 wt % theoretical loading of Au. Subsequently, the sodium carbonate solution (20 mL, 1.2 equiv) was then slowly added to the above suspension, and the mixture was stirred for 4 h. The as-prepared catalyst was washed with deionized water until the washings contained no residual chloride ions (as shown by the absence of precipitation with the $AgNO_3$ solution). Then, the samples were dried at 60 °C in an oven for 8 h. Finally, the as-prepared catalyst was pretreated in a muffle furnace at 300 °C with a heating rate of 5 °C min^{-1} for 2 h. The resulting catalysts are denoted as Au/ZnO. Other supported Au catalysts were prepared using similar procedures.

2.4. Procedure for the CO Coupling to Oxamides in a Batch Reactor. An amine (0.25 mmol), Au/ZnO (2 mol %), and toluene (3.0 mL) were loaded into a batch reactor containing a Teflon-coated magnetic stirring bar (WATTCAS Schlenk Autoclave, WP-MSAR-250A). The batch reactor was successively charged with 0.1 MPa air and 0.4 MPa CO. (*Caution*: The lower and upper explosive limits of CO and atmospheric pressure are, respectively, 12.5 and 74.2% by volume of air.) The mixture was stirred at room temperature for 12 h. Afterward, the reaction was stopped and the pressure was carefully released. The yields of oxamides were determined by GC (Agilent 7820A equipped with an FID detector) using dodecane as the calibrated internal standard. The gas phase was determined by GC (Agilent 7890B equipped with FID and TCD detectors).

2.5. Flow Reactor. Evaluation of the catalytic stability was carried out in a homemade evaluation device. Au/ZnO (1.0 g,1 wt %) was calcined at 300 °C for 2 h under an air atmosphere. Subsequently, the catalysts were packed in a 20 mm quartz tube (internal diameter, 8 mm). The reactant (50 mmol of morpholine in 500 mL of toluene) was pumped into the reactor at a liquid hourly space velocity (LHSV) of 1.5 h^{-1} mixing with the CO and air mixture (4:1) at a gas hourly space velocity (GHSV) of 0.12 h^{-1}. The catalyst tests were carried out at 1 atm of CO and air mixture. The conversion of morpholine and selectivity of oxamides were determined by GC (Agilent 7820A equipped with the FID detector).

2.6. Characterizations. ICP measurements were conducted with an Agilent 720ES (OES). Surface chemical analysis was conducted by X-ray photoelectron spectroscopy (Thermo Scientific K-Alpha). The binding energy (BE) values were calibrated against the carbon 1s signal (BE = 284.8 eV) of contaminant carbon. The X-ray absorption fine structure (XAFS) spectra of the Au L_{III} edge were acquired at the BL14W beamline of the Shanghai Synchrotron Radiation Facility (SSRF). Aberration-corrected high-angle annular dark-field scanning transmission electron microscopy (ac-HAADF-STEM), electron energy loss spectroscopy (EELS), and linear element energy-dispersive spectroscopy (EDS) measurements were acquired with a JEOL JEM ARM200F with a Cs-corrected probe operated at 200 or 80 kV. *In situ* Fourier transform infrared spectroscopy experiments were performed on a Nicolet iS50 FTIR spectrometer with 32 scans at a 4 cm^{-1} resolution at room temperature. A liquid nitrogen-cooled MCT detector was used. A specific amount of Au/MO_x was placed in the cell with a ZnSe window. After each CO adsorption round of Au-based catalysts, the sample was purged with N_2 for 1 h at 200 °C to desorb the adsorbed H_2O or volatile pollutants, and the background spectrum was recorded after cooling to room temperature. Then, a mixture gas of 5% CO/N_2 was introduced into the reaction cell with a rate of 30 mL min^{-1}, and the CO-DRIFT spectrum was collected until the sample was saturated adsorbed by CO. For the coadsorption of CO and DMA over Au/ZnO catalysts, Au/ZnO was saturated adsorbed by CO. Later, a mixture gas of DMA/CO/N_2 was introduced into the reaction cell with a rate of 30 mL min^{-1} and the DRIFT spectrum was collected. Finally, synthetic air was also introduced into the reaction cell and the spectral change was monitored.

2.7. Theoretical Calculation. The active site structures were determined by scanning the global potential energy surface of $Au_aZn_bO_c$/ZnO using the SSW-NN method, as implemented in the large-scale atomic simulation with neural network potential (LASP) code.[31,32] The Au−Zn−O PES describes the global neural network (G-NN) potential that was obtained by self-learning the dataset produced from SSW global optimization. The G-NN potential is available from the LASP project (www.lasphub.com). More details on SSW-NN and the Au−Zn−O G-NN potential are provided in the Supporting Information.

In the SSW-NN simulation, the ZnO $(10\bar{1}0)$ surface is modeled by a three-layer slab, where the bottom two layers were fixed at the bulk-truncated position and the top layer was allowed to relax. The active site model $Au_{22}Zn_8O_{10}$/ZnO identified from SSW-NN contains a $Au_{22}Zn_8O_{10}$ cluster grown on the ZnO$(10\bar{1}0)$ surface, and the supercell has a dimension of 19.49 × 20.82 $Å^2$ for the surface.

The reaction pathways on the $Au_{22}Zn_8O_{10}$/ZnO active site were calculated using first-principles DFT as implemented in the Vienna Ab initio Simulation Package (VASP).[33] The exchange−correlation functional utilized was GGA-PBE. The electron−ion interaction was represented by the projector-augmented-wave pseudopotential, and the kinetics energy cutoff utilized was 450 eV. All of the reaction TSs were determined using the constrained Broyden dimer (CBD) method,[34,35] and the TS was further confirmed by the

https://doi.org/10.1021/acscatal.2c05358
ACS Catal. 2023, 13, 735−743

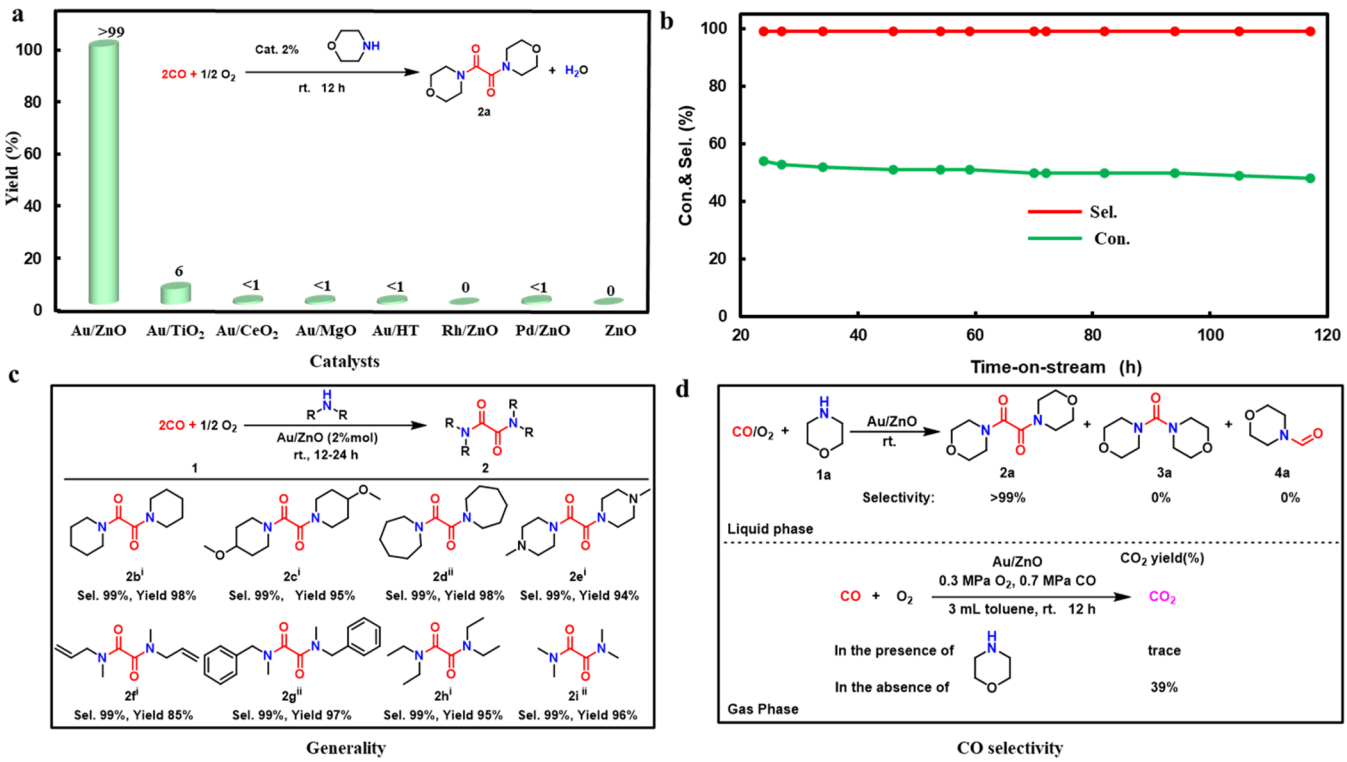

Figure 1. Catalytic performance in oxidative CO coupling to oxamides at room temperature. (a) Screening of catalysts in oxidative coupling of CO to oxamides (reaction conditions: morpholine (0.25 mmol), toluene (3 mL), air (0.1 MPa), CO (0.4 MPa), Au/MO_x, and M/ZnO (2 mol %)). (b) Stability test in a fixed-bed reactor at atmospheric pressure. (c) Generality of excellent activity and selectivity (reaction time i. 24 h; ii. 12 h). (d) Excellent selectivity in both the liquid and gas phase (*N* balance > 97%).

vibrational frequency analysis and the geometry extrapolation to the neighboring minima.

Microkinetic simulation was performed to evaluate the theoretical turnover frequency (TOF) and to identify the apparent activation energy. In the simulation, the pressure of O_2 and CO was fixed under the reaction conditions (298 K, 0.1 MPa air, 0.4 MPa CO) to simulate a fluidized-bed catalytic reactor, and the temperature was set in a range from 295 to 315 K.

3. RESULTS AND DISCUSSION

3.1. Catalytic Performance. Catalyst screening was initially performed to identify the most active ensemble by varying the composition of a metal/oxide-supported catalyst using morpholine as the model substrate in a batch reactor. Importantly, the Au/ZnO catalyst was prominent with the oxamide yield being >99% at room temperature, which is exceptional in comparison with other supported metal catalysts (Figure 1a and Table S1 in the Supporting Information). Au supported on other materials was investigated, and it was found that Au/TiO_2 has a sluggish performance (6% yield), and Au/MgO, Au/CeO_2, and Au/HT are essentially inactive under such mild conditions.[36] If Au metal is replaced, as in Pd/ZnO or Rh/ZnO, little or no activity was observed. To examine the heterogeneous nature of the Au/ZnO catalyst, we separated the solid catalyst by filtration, and inductively coupled plasma (ICP) analysis showed that no Au could be detected in the filtrate. In addition, the reaction is terminated after the removal of Au/ZnO catalysts when the oxamide yield reaches approximately 40% (Supporting Information, Figure S3).

A continuous flow reactor was then utilized to take full advantage of the high catalytic activity and selectivity of the heterogeneous Au/ZnO catalyst. Our long-term duration tests showed that the reaction can go smoothly at atmospheric pressure with a medium conversion (∼50%) for ∼120 h and near quantitive selectivity to oxamide (Figure 1b). A scaled-up reaction of CO with morpholine (50 mmol) with 0.1 mol % Au was carried out and showed that the yield to the target oxamide is 86% at room temperature (Supporting Information, Figure S4). Figure 1c shows the applicability of the Au/ZnO catalyst to other secondary amines, such as piperidine, 4-methoxypiperidine, 1-methylpiperazine, *N*-allylmethylamine, *N*-methylbenzylamine, and dimethylamine. All of these structurally diverse amines were found to follow the same pattern, yielding the corresponding oxamides with a high yield and high selectivity. But, unfortunately, the aromatic amines, such as *N*-methyl aniline and aniline, were inactive over the Au/ZnO catalyst (Supporting Information, Figure S5).

No trace of urea or formamide compounds, the byproducts frequently formed in the oxidative carbonylation, was detected in the reaction (Figure 1d).[37−41] In the meantime, CO oxidation[42−45] is fully inhibited in the presence of amines, such as morpholine, whereas the yield of CO_2 *via* CO oxidation is 39% in the control experiment without the addition of amine, which indicates the CO oxidation and oxidative CO coupling probably compete for the same active site on the Au/ZnO catalyst.

3.2. Characterization of the Structure and Electronic State of Au/ZnO Catalysts. Using X-ray photoelectron spectroscopy (XPS) to follow the catalyst preparation, as shown in Figure 2a, we found that the cationic Au precursor turns into a near-metallic state after calcination.[46−49] We then

https://doi.org/10.1021/acscatal.2c05358
ACS Catal. 2023, 13, 735−743

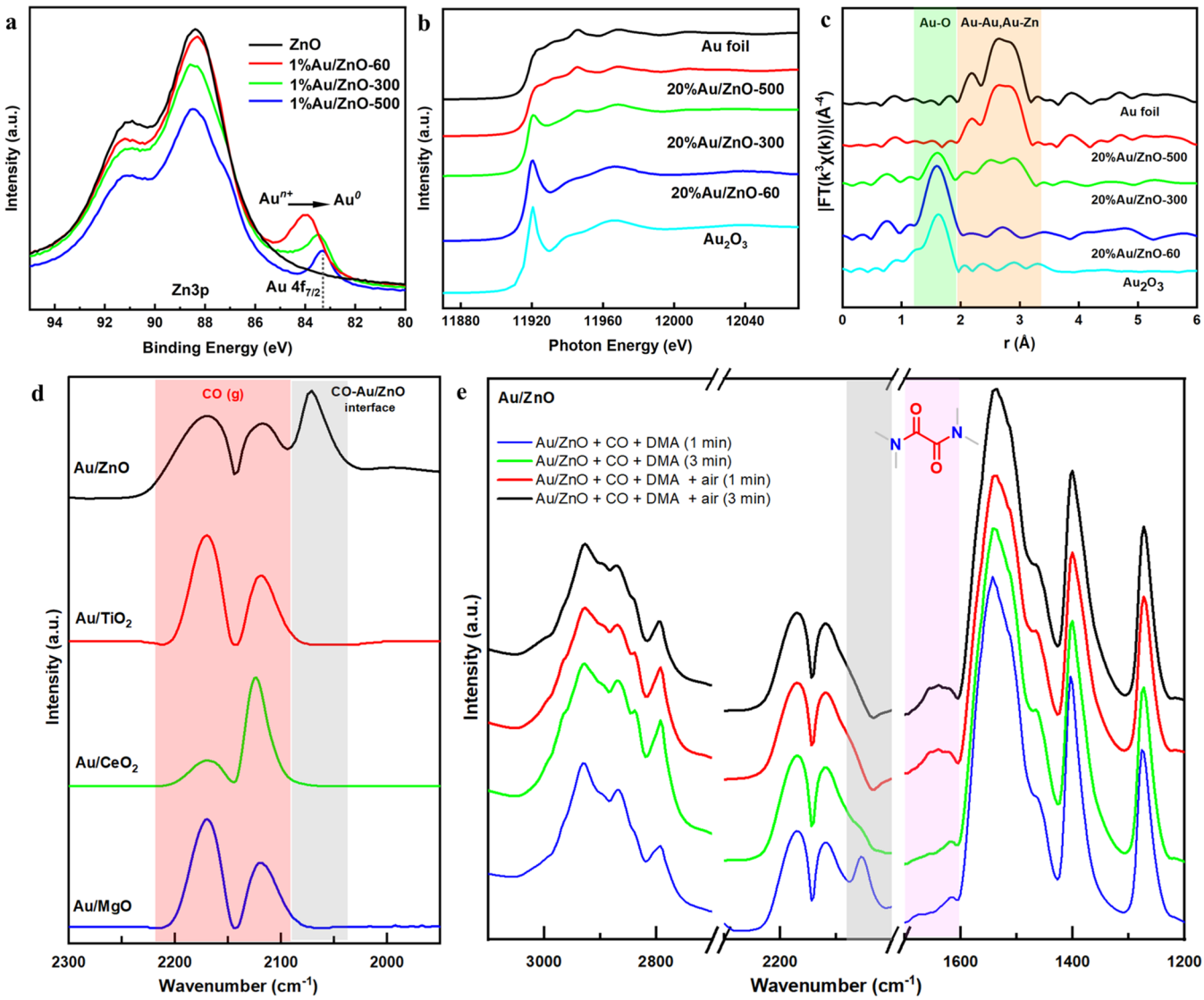

Figure 2. Characterization results of Au/ZnO. (a) X-ray photoelectron spectra of Zn 3p and Au $4f_{7/2}$; (b) normalized XANES spectra at the Au L_3-edge of 20%Au/ZnO catalyst; (c) corresponding Fourier transform of k^3-weighted EXAFS spectra for 20%Au/ZnO, Au foil, and Au_2O_3; (d) *in situ* DRIFT spectra of CO adsorption over Au/ZnO, Au/TiO_2, Au/CeO_2, and Au/MgO samples; (e) coadsorption of CO/DMA/air over Au/ZnO.

investigated the electronic structure of various catalysts by X-ray absorption spectroscopy (XAS). The loading of Au was increased from 1 to 20% to achieve a better S/N ratio and eliminate the partial overlap of the Au L_3-edge on the Zn K-edge (Supporting Information Figure S8).[50,51] The L_3-edge X-ray absorption near-edge structure (XANES) spectra were measured for the calcined and noncalcined samples under an air atmosphere at 300 or 500 °C, with Au foil and Au_2O_3 as reference samples (Figure 2b). In the noncalcined Au/ZnO, an adsorption edge appeared at ∼11,919 eV in the Au L_3-edge XANES spectra, which is a characteristic of gold oxide. After calcination at 300 °C, new peaks appeared at ∼11,946 and ∼11,968 eV in the Au L_3-edge XANES spectra, suggesting the formation of Au^0. After further calcination at 500 °C, the oxide peak disappears from the XANES spectra of Au/ZnO (500 °C) and the fingerprinting features of the spectrum are similar to that of Au foil.[52] Extended X-ray absorption fine structure (EXAFS) spectra were used to determine the local coordination environment of the Au/ZnO catalysts. As shown in the Fourier transform of k^3-weighted EXAFS spectra in Figure 2c, there are three major peaks at 1.97, 2.85, and 3.11 Å, which is attributed to Au−O (with a coordination number, 1.4), Au−Au (with a coordination number, 7.7), and Au−Zn (with a coordination number, 2.2) in the Au/ZnO-300 catalyst (Supporting Information, Table S2 and Figure S7).[50,51,53] The presence of Au−O, Au−Zn, and relatively little scattered Au−Au in the Au/ZnO catalyst can be explained by the formation of an Au−ZnO interface structure.

The interfacial structure of Au−ZnO is further confirmed by CO adsorption Fourier transform infrared spectroscopy (FTIR) experiments. Prior to the reaction, CO adsorption has three large bands at 2170, 2121, and 2070 cm^{-1} (Figure 2d, Supporting Information, Figures S9−S11).[54,55] The first two bands are the signals of gaseous and chemisorbed CO, and the third is assigned to Au−CO species formed at low-coordinated metallic (Au^0) sites that are abundant around the Au/ZnO interface.[56−59] As shown in Figure 2d, for other Au/MO_x catalysts, such as Au/TiO_2, Au/MgO, and Au/CeO_2, no CO adsorption peak at around 2070 cm^{-1} can be observed after introduction of CO into the reaction system, indicating

https://doi.org/10.1021/acscatal.2c05358
ACS Catal. 2023, 13, 735−743

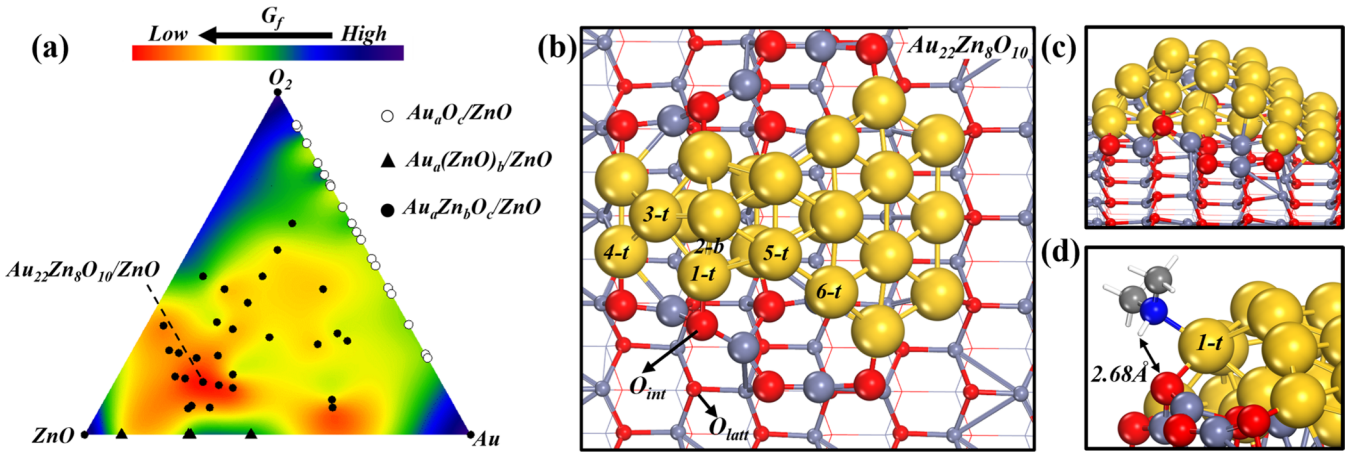

Figure 3. Structure of the Au/ZnO interfacial active site from machine learning atomic simulation. (a) Au−Zn−O ternary phase diagram under catalyst preparation conditions determined from the SSW-NN global structure search. The color bar represents the energy level of G_f as defined in eq S11 (SI) and the black dots represent the composition ($Au_aZn_bO_c$) that was studied. (b) Atomic structure of $Au_{22}Zn_8O_{10}$/ZnO and the adsorption site (t: top site, b: bridge site). (c) Side view of the structure. (d) Most stable adsorption configuration of DMA. The color scheme for atoms is Au: yellow ball; Zn: silver gray ball; O: red ball; H: white ball; N: blue ball; C: gray ball.

that the CO is adsorbed only with difficulty at the Au sites of Au/TiO_2, Au/MgO, and Au/CeO_2 catalysts. Consequently, poor or nonactivity for the CO oxidative coupling highlights the importance of the unique Au−ZnO interfacial structure for the oxidative coupling process of CO.

For the Au/ZnO catalyst, when we introduce the DMA and CO mixture into the IR cell, the CO band at the Au interfacial sites (2070 cm^{-1}) decreases and then gradually disappears. New bands appear at 2800−3000 and 1400−1600 cm^{-1} and correspond to the C−H and N−H stretching of the adsorbed DMA molecules, respectively.[60−62] This suggests that DMA can replace CO to be adsorbed at the Au−ZnO interfacial sites, in agreement with the theoretical results (Figure 2e, Supporting Information Figure S11). By further pumping air into the reaction system, the characteristic peak for the carbonyl group of oxamides (using the standard tetramethyl oxamide as a reference, Supporting Information, Figure S12) appears at 1690−1610 cm^{-1}. Its proportion increases in oxygen and no other intermediate species can be identified. Those *in situ* diffused reflectance infrared Fourier transform spectroscopy (DRIFTS) results clearly demonstrate that the importance of the Au−ZnO interfacial structure in the direct coupling reaction of CO and the air is used to produce oxamide.

We also attempted to observe the Au/ZnO interface by high-resolution transmission electron microscopy (TEM). The TEM images obtained show that the average size of Au nanoparticles is 4 nm, but smaller Au nanoparticles, ca. ∼1 nm, were also identified (see the Supporting Information, Figures S13−S15). The microregion electron energy loss spectroscopy (μ-EELS) spectra and linear-scan energy-dispersive spectroscopy of 1% Au/ZnO demonstrates the presence of the O K-edge and Zn L-edge signals on the particle surfaces, confirming that Au nanoparticles can reconstruct the ZnO surface and the extra Zn and O atoms exist at the edge of Au nanoparticles (Supporting Information, Figure S13e,f).

3.3. Au/ZnO Interfacial Active Site Structure by Machine Learning Atomic Simulation. To reveal the structure of the interfacial active site and better understand the reaction, we utilized our recently developed large-scale machine learning atomic simulation to examine the thermodynamics of the Au−ZnO system under oxidative conditions. The global minima (GM) were explored of a series of differently sized Au particles (≤52 atoms) supported on ZnO(10$\bar{1}$0), the most stable surface of ZnO, using the stochastic surface walking (SSW)[63] global optimization based on an Au−Zn−O ternary global neural network (G-NN)[64] potential (see the Supporting Information for the details of SSW-NN simulations). Since Au nanoparticles may cause reconstruction of the ZnO surface and thus lead to a nonstochiometric Zn/O ratio on the surface, our simulations have considered extra Zn and O atoms to support Au nanoparticles beyond the Zn/O = 1:1 stoichiometry. The model is denoted as $Au_aZn_bO_c$/ZnO, where superscripts *a*, *b*, and *c* are the number of surface Au, Zn, and O atoms, respectively. More than 50 compositions with different values of *a*, *b*, and *c* were explored by SSW-NN, as indicated by the black points in Figure 3a, and the corresponding GM were obtained after examining more than 100,000 minima at each composition. The low-energy structures have been further checked by DFT calculations (Supporting Information, Table S4).

Using the global minima, we were able to compute the free energy of formation of $Au_aZn_bO_c$/ZnO, G_f in eV per Au atom with respect to the ZnO stoichiometric surface, the Au(111) surface, and the gas phase O_2 under the conditions of catalyst preparation (eq S12 in the Supporting Information), and the thermodynamics phase diagram that was obtained is shown in Figure 3a. It can be seen that $Au_{22}Zn_8O_{10}$/ZnO is the most stable composition with G_f = −0.044 eV, while the bare Au_a/ZnO without additional Zn or O ions is generally much less stable with G_f > 0. Close inspection of the $Au_{22}Zn_8O_{10}$/ZnO structure, depicted in Figure 3b,c, showed that half of the Au_{22}, on the right-hand side, is largely in the close-packed form with the (111) face exposed, where its right terminus sits directly above the ZnO support; more interestingly, the other half of Au_{22} has a five-fold axis and interacts strongly with two nearby symmetric Zn_4O_5 moieties. For the $Au_{22}Zn_8O_{10}$/ZnO, the average coordination numbers of the interface Au with their neighboring O, Zn, and the average coordination of Au with other Au atoms in the cluster are 1.0, 2.0, and 4.5, respectively. In total, there are eight Au−O bonds and twelve Zn−Au bonds

https://doi.org/10.1021/acscatal.2c05358
ACS Catal. 2023, 13, 735−743

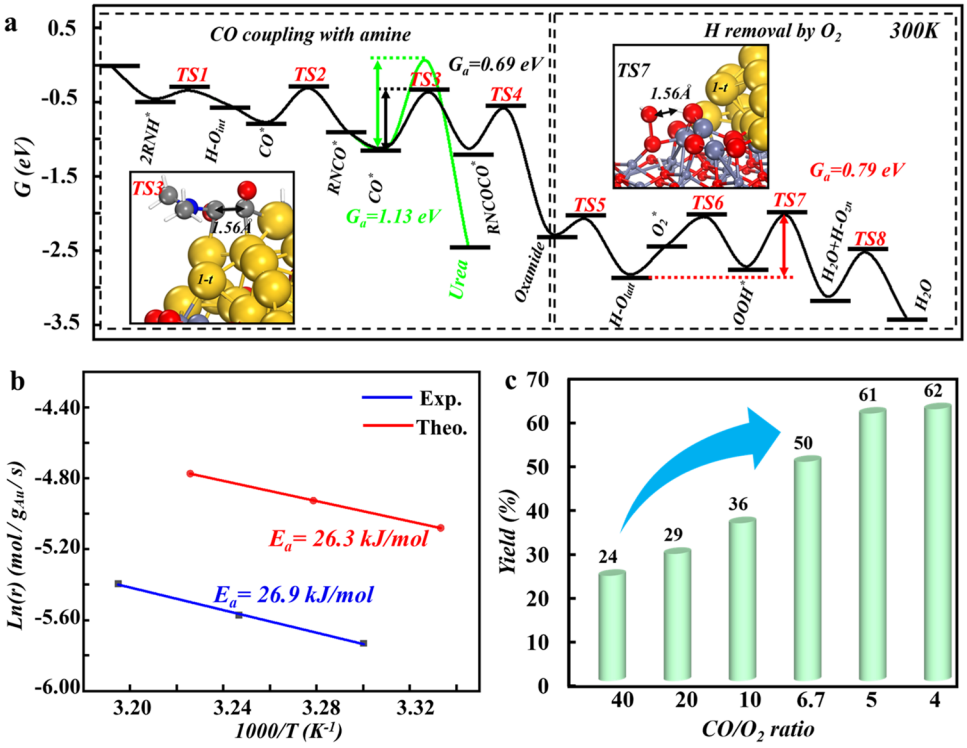

Figure 4. Gibbs free energy profiles of the reaction pathway and reaction kinetics. (a) Energy profile for the CO coupling with amine, the energy profile for the CO coupling with amine and the H removal by O_2. The side reaction to urea is also shown in the green curve. The inset pictures represent the key reaction transition states. R_2NH^* represents the adsorbed amine (R = $(CH_3)_2$). (b) Arrhenius plots of the oxidative CO coupling to oxamides from microkinetics simulations (red) and that from the experiment. Reaction conditions: morpholine (0.25 mmol), Au/ZnO (2 mol %), air (0.1 MPa), CO (0.4 MPa), toluene (3 mL) reaction time 3 h; (c) yield vs the CO/O_2 ratio, showing the effect of oxygen content on the activity. Reaction conditions: morpholine (0.25 mmol), Au/ZnO (2 mol %), CO (0.4 MPa), and N_2/O_2 mixture (0.1 MPa), toluene (3 mL) reaction time 3 h at room temperature.

at the Au/ZnO interface, revealing a variety of possible adsorption sites for molecules.

Density functional theory (DFT) calculations were employed to characterize the bonding nature in these interfacial sites using CO and dimethylamine (DMA) as probe molecules. We found that DMA molecules prefer to adsorb at the interfacial cationic Au site of Au/ZnO with its N end, namely, **1-t** site in Figure 3d. The adsorption energy of DMA on all interfacial sites, including **1-t**, **3-t**, and **6-t** sites (Figure 3b), is quite similar, all at approximately −0.7 eV. Upon its adsorption, CO tends to occupy the low-coordinated Au sites, and the most stable adsorption site is the bridging site **2-b** (−1.03 eV), which is ∼4 Å away from the nearest interfacial O atom (see Figure 3b).[65] CO can also be adsorbed at the **1-t** Au site (−0.43 eV), but the product is much less stable than that involving DMA (−0.73 eV), suggesting that CO cannot compete with DMA in occupying the interfacial cationic Au sites.[66] Even after DMA adsorption at the **1-t** site, CO can still be coadsorbed at the nearby **2-b** site with an adsorption energy of −0.76 eV. By comparing DMA and CO adsorption at the interfacial sites, we expect that DMA molecules can occupy almost all exposed interfacial sites, which are the active site to form oxamides. The removal of CO from the interfacial site prohibits effectively CO oxidation with the interfacial O atoms, as confirmed in the experiment.

3.4. Reaction Mechanism and Microkinetic Simulation. The reaction pathways for CO coupling with amine were examined by DFT calculations, and the reaction profile is shown in Figure 4a (more reaction snapshots are shown in the Supporting Information, Figures S16−S18). The reaction starts with the facile dehydrogenation of an adsorbed DMA to the nearby interfacial O (O_{int}) of Zn_8O_{10} (dh-DMA). The dh-DMA then reacts with a nearby adsorbed CO overcoming a free energy barrier of 0.45 eV to form an amide complex (TS2 in Figure 4), which can then couple with another CO with a barrier of 0.69 eV (TS3 in Figure 4a), ultimately yielding a dicarbonyl intermediate. This dicarbonyl intermediate combines with another dh-DMA to produce oxamide with a barrier of 0.51 eV. For each oxamide formation, two H* species are left as H−O_{int} at the O_{int} sites, and their diffusion to the nearby lattice O of ZnO support (O_{latt}) site is exothermic by 0.59 eV per H with a low barrier of 0.14 eV (TS5 in Figure 4a). The unoccupied O_{int} sites are then available for a second oxamide formation. The O_{int} is thus the active site for oxamide formation, while the O_{latt} acts as the reservoir for H.

The O_2 is necessary to reactivate the catalyst by removing the H left by the DMA dehydrogenation at the O_{int} site. As shown in Figure 4a (the reaction snapshots are shown in the Supporting Information, Figure S16), an incoming O_2 molecule can be weakly adsorbed at the top site of the Zn of ZnO support, designated O−O_{Zn} with −0.39 eV adsorption free energy. This O_2* reacts sequentially with two H*−O_{int} to form a H_2O molecule, and the left bridging O on Zn (O_{Zn}) acquires the H from the nearby O_{latt}. This H−O_{Zn} will desorb as H_2O after accepting H from H*−O_{int}. The highest energy barrier is at the OOH* + H−O_{int} step (TS7), which has a free energy barrier of 0.79 eV.

https://doi.org/10.1021/acscatal.2c05358
ACS Catal. 2023, 13, 735−743

Based on the DFT kinetics data, microkinetic simulations were performed to obtain the reaction rate at different temperatures, from which the apparent reaction barrier can be deduced from an Arrhenius plot. The OOH* + H−O_{int} step in the H removal pathway was found to be the rate-determining step, and the apparent barrier between 295 and 320 K is only 0.27 eV (26.3 kJ mol^{-1}), in good agreement with the experimentally measured apparent activation energies (26.9 kJ mol^{-1}), as shown in Figure 4b. Importantly, our microkinetic simulation predicts that the rate of oxamide formation can be significantly accelerated if the chemical potential of O_2 is elevated: with the oxygen partial pressure increased by 4 times, the reaction rate should double. The entropy loss causes the O_2 in the gas phase (−0.59 eV) being more stable than its adsorbed state (−0.20 eV), and thus, the adsorption endothermicity contributes to the overall reaction barrier (Figure 4a). By elevating the partial pressure of O_2 to reduce the endothermicity, the reaction can be speeded up. Experimentally, we then carefully examined the effect of oxygen partial pressure on the catalytic reaction and found that upon replacing air with O_2 at higher pressures, the reaction rate increases up to 2.1 times (Figure 4c), supporting the theoretical prediction.

4. CONCLUSIONS

This work has achieved the first example of room-temperature CO oxidative coupling to oxamide with high selectivity and stability in a fixed-bed flow reactor. By combining machine learning atomic simulation and experimental characterization techniques, the Au/ZnO catalyst was shown to have strong metal−support interactions, featuring an Au−ZnO_x/ZnO (x > 1) interface structure. Despite the presence of three reactants (CO, O_2, and an amine), the synergy of Au nanoparticles, ZnO_x linkage, and ZnO support allows dehydrogenation of the amine, CO coupling, and H removal by O_2 to occur sequentially with an apparent low barrier (26 kJ mol^{-1}). The atomic level knowledge revealed here of the interfacial catalysis should assist the future design of better heterogeneous catalysts for production of value-added chemicals under mild conditions.

■ ASSOCIATED CONTENT

Supporting Information

The Supporting Information is available free of charge at https://pubs.acs.org/doi/10.1021/acscatal.2c05358.

Experimental section; additional material characterizations; and theoretical calculations (PDF)

■ AUTHOR INFORMATION

Corresponding Authors

Ding Ma − *College of Chemistry and Molecular Engineering and College of Engineering, Peking University, Beijing 100871, China;* orcid.org/0000-0002-3341-2998; Email: dma@pku.edu.cn

Zhi-Pan Liu − *Collaborative Innovation Center of Chemistry for Energy Material, Shanghai Key Laboratory of Molecular Catalysis and Innovative Materials, Key Laboratory of Computational Physical Science, Department of Chemistry, Fudan University, Shanghai 200433, China;* orcid.org/0000-0002-2906-5217; Email: zpliu@fudan.edu.cn

Lin He − *State Key Laboratory for Oxo Synthesis and Selective Oxidation, Lanzhou Institute of Chemical Physics (LICP), Chinese Academy of Sciences, Lanzhou 730000, China;* orcid.org/0000-0001-7437-1443; Email: helin@licp.cas.cn

Authors

Yanwei Cao − *State Key Laboratory for Oxo Synthesis and Selective Oxidation, Lanzhou Institute of Chemical Physics (LICP), Chinese Academy of Sciences, Lanzhou 730000, China; Collaborative Innovation Center of Chemistry for Energy Material, Shanghai Key Laboratory of Molecular Catalysis and Innovative Materials, Key Laboratory of Computational Physical Science, Department of Chemistry, Fudan University, Shanghai 200433, China*

Yao Peng − *Collaborative Innovation Center of Chemistry for Energy Material, Shanghai Key Laboratory of Molecular Catalysis and Innovative Materials, Key Laboratory of Computational Physical Science, Department of Chemistry, Fudan University, Shanghai 200433, China*

Danyang Cheng − *College of Chemistry and Molecular Engineering and College of Engineering, Peking University, Beijing 100871, China*

Lin Chen − *Collaborative Innovation Center of Chemistry for Energy Material, Shanghai Key Laboratory of Molecular Catalysis and Innovative Materials, Key Laboratory of Computational Physical Science, Department of Chemistry, Fudan University, Shanghai 200433, China*

Maolin Wang − *College of Chemistry and Molecular Engineering and College of Engineering, Peking University, Beijing 100871, China*

Cheng Shang − *Collaborative Innovation Center of Chemistry for Energy Material, Shanghai Key Laboratory of Molecular Catalysis and Innovative Materials, Key Laboratory of Computational Physical Science, Department of Chemistry, Fudan University, Shanghai 200433, China;* orcid.org/0000-0001-7486-1514

Lirong Zheng − *Beijing Synchrotron Radiation Facility (BSRF), Institute of High Energy Physics, Chinese Academy of Sciences, Beijing 100049, China*

Complete contact information is available at: https://pubs.acs.org/10.1021/acscatal.2c05358

Author Contributions

[⊥]Y.C., Y.P., and D.C. contributed equally to this work.

Notes

The authors declare no competing financial interest.

The software codes for large-scale atomic simulation with neural network potential and the NN potentials used within the article are available from the corresponding authors upon request or on the website http://www.lasphub.com.

■ ACKNOWLEDGMENTS

This work received financial support from the National Key Research and Development Program of China (2017YFB0602200, 2018YFA0208600), National Natural Science Foundation of China (21802151, 21972152, 21932002, 12188101, 22033003, 91945301, 91745201, 92145302, 22122301, and 92061112), the China Postdoctoral Science Foundation (2020M681146), and the Tencent Foundation for XPLORER PRIZE. XAS was conducted at the Beijing Synchrotron Radiation Facility (BSRF) and the Shanghai Synchrotron Radiation Facility (SSRF).

DEDICATION

This paper is dedicated to Professor Matthias Beller on the occasion of his 60th birthday.

REFERENCES

(1) Peng, J.-B.; Geng, H.-Q.; Wu, X.-F. The Chemistry of CO: Carbonylation. *Chem* **2019**, *5*, 526−552.

(2) Chen, Y.; Wei, J.; Duyar, M. S.; Ordomsky, V. V.; Khodakov, A. Y.; Liu, J. Carbon-based catalysts for Fischer-Tropsch synthesis. *Chem. Soc. Rev.* **2021**, *50*, 2337−2366.

(3) Liu, Q.-Y.; Shang, C.; Liu, Z.-P. In Situ Active Site for Fe-Catalyzed Fischer-Tropsch Synthesis: Recent Progress and Future Challenges. *J. Phys. Chem. Lett.* **2022**, *13*, 3342−3352.

(4) Wolf, M.; Fischer, N.; Claeys, M. Formation of metal-support compounds in cobalt-based Fischer-Tropsch synthesis: A review. *Chem Catal.* **2021**, *1*, 1014−1041.

(5) Rahmati, M.; Safdari, M.-S.; Fletcher, T. H.; Argyle, M. D.; Bartholomew, C. H. Chemical and Thermal Sintering of Supported Metals with Emphasis on Cobalt Catalysts During Fischer-Tropsch Synthesis. *Chem. Rev.* **2020**, *120*, 4455−4533.

(6) Kang, J.; He, S.; Zhou, W.; Shen, Z.; Li, Y.; Chen, M.; Zhang, Q.; Wang, Y. Single-pass transformation of syngas into ethanol with high selectivity by triple tandem catalysis. *Nat. Commun.* **2020**, *11*, No. 827.

(7) Summerscales, O. T.; Cloke, F. G. N.; Hitchcock, P. B.; Green, J. C.; Hazari, N. Reductive Cyclotrimerization of Carbon Monoxide to the Deltate Dianion by an Organometallic Uranium Complex. *Science* **2006**, *311*, 829−831.

(8) Wayland, B.; Fu, X. Building Molecules with Carbon Monoxide Reductive Coupling. *Science* **2006**, *311*, 790−791.

(9) Zhang, Q.; Kang, J.; Wang, Y. Development of Novel Catalysts for Fischer-Tropsch Synthesis: Tuning the Product Selectivity. *ChemCatChem* **2010**, *2*, 1030−1058.

(10) Wang, P.; Chen, W.; Chiang, F.-K.; Dugulan, A. I.; Song, Y.; Pestman, R.; Zhang, K.; Yao, J.; Feng, B.; Miao, P.; Xu, W.; Hensen, E. J. M. Synthesis of stable and low-CO_2 selective ε-iron carbide Fischer-Tropsch catalysts. *Sci. Adv.* **2018**, *4*, No. eaau2947.

(11) Freund, H. J.; Meijer, G.; Scheffler, M.; Schlogl, R.; Wolf, M. CO oxidation as a prototypical reaction for heterogeneous processes. *Angew. Chem., Int. Ed.* **2011**, *50*, 10064−10094.

(12) van Spronsen, M. A.; Frenken, J. W. M.; Groot, I. M. N. Surface science under reaction conditions: CO oxidation on Pt and Pd model catalysts. *Chem. Soc. Rev.* **2017**, *46*, 4347−4374.

(13) Lin, J.; Wang, X.; Zhang, T. Recent progress in CO oxidation over Pt-group-metal catalysts at low temperatures. *Chin. J. Catal.* **2016**, *37*, 1805−1813.

(14) Li, C. W.; Ciston, J.; Kanan, M. W. Electroreduction of carbon monoxide to liquid fuel on oxide-derived nanocrystalline copper. *Nature* **2014**, *508*, 504−507.

(15) Wang, X.; Wang, Z.; Zhuang, T. T.; Dinh, C. T.; Li, J.; Nam, D. H.; Li, F.; Huang, C. W.; Tan, C. S.; Chen, Z.; Chi, M.; Gabardo, C. M.; Seifitokaldani, A.; Todorovic, P.; Proppe, A.; Pang, Y.; Kirmani, A. R.; Wang, Y.; Ip, A. H.; Richter, L. J.; Scheffel, B.; Xu, A.; Lo, S. C.; Kelley, S. O.; Sinton, D.; Sargent, E. H. Efficient upgrading of CO to C_3 fuel using asymmetric C-C coupling active sites. *Nat. Commun.* **2019**, *10*, No. 5186.

(16) Jiang, M.-P.; Huang, K.-K.; Liu, J.-H.; Wang, D.; Wang, Y.; Wang, X.; Li, Z.-D.; Wang, X.-Y.; Geng, Z.-B.; Hou, X.-Y.; Feng, S.-H. Magnetic-Field-Regulated TiO_2 {100} Facets: A Strategy for C-C Coupling in CO_2 Photocatalytic Conversion. *Chem* **2020**, *6*, 2335−2346.

(17) Hiwatari, K.; Kayaki, Y.; Okita, K.; Ukai, T.; Shimizu, I.; Yamamoto, A. Selective Oxidative Carbonylation of Amines to Oxamides and Ureas Catalyzed by Palladium Complexes. *Bull. Chem. Soc. Jpn.* **2004**, *77*, 2237−2250.

(18) Dong, K.; Elangovan, S.; Sang, R.; Spannenberg, A.; Jackstell, R.; Junge, K.; Li, Y.; Beller, M. Selective catalytic two-step process for ethylene glycol from carbon monoxide. *Nat. Commun.* **2016**, *7*, No. 12075.

(19) Lu, L.; Qiu, F.; Alhumade, H.; Zhang, H.; Lei, A. Tuning the Oxidative Mono- or Double-Carbonylation of Alkanes with CO by Choosing a Co or Cu Catalyst. *ACS Catal.* **2022**, *12*, 9664−9669.

(20) Li, W.; Duan, Z.; Zhang, X.; Zhang, H.; Wang, M.; Jiang, R.; Zeng, H.; Liu, C.; Lei, A. From Anilines to Isatins: Oxidative Palladium-Catalyzed Double Carbonylation of C H Bonds. *Angew. Chem.* **2015**, *127*, 1913−1916.

(21) Meyer, T.; Rabeah, J.; Brückner, A.; Wu, X.-F. Visible-Light-Induced Palladium-Catalyzed Dehydrogenative Carbonylation of Amines to Oxalamides. *Chem. - Eur. J.* **2021**, *27*, 5642−5647.

(22) Gadge, S. T.; Bhanage, B. M. Pd/C-Catalyzed Synthesis of Oxamates by Oxidative Cross Double Carbonylation of Amines and Alcohols under Co-catalyst, Base, Dehydrating Agent, and Ligand-Free Conditions. *J. Org. Chem.* **2013**, *78*, 6793−6797.

(23) Mancuso, R.; Raut, D. S.; Della Ca, N.; Fini, F.; Carfagna, C.; Gabriele, B. Catalytic Oxidative Carbonylation of Amino Moieties to Ureas, Oxamides, 2-Oxazolidinones, and Benzoxazolones. *ChemSusChem* **2015**, *8*, 2204−2211.

(24) Satapathy, A.; Gadge, S. T.; Bhanage, B. M. An Improved Strategy for the Synthesis of Ethylene Glycol by Oxamate-Mediated Catalytic Hydrogenation. *ChemSusChem* **2017**, *10*, 1356−1359.

(25) Murahashi, S.-I.; Mitsue, Y.; Ike, K. Palladium-catalysed cross double carbonylation of amines and alcohols: synthesis of oxamates. *J. Chem. Soc., Chem. Commun.* **1987**, 125−127.

(26) Mukherjee, T.; Zhang, Y.; Abdelwahed, S.; Ealick, S. E.; Begley, T. P. Catalysis of a Flavoenzyme-Mediated Amide Hydrolysis. *J. Am. Chem. Soc.* **2010**, *132*, 5550−5551.

(27) Sayre, L. M. Metal ion catalysis of amide hydrolysis. *J. Am. Chem. Soc.* **1986**, *108*, 1632−1635.

(28) Zhang, X.; Luo, K.; Chen, W.; Wang, L. Amide Hydrolysis Reaction Catalyzed by KF/Al_2O_3 under Microwave Irradiation and Solvent Free Conditions. *Chin. J. Chem.* **2011**, *29*, 2209−2212.

(29) Mitsudome, T.; Noujima, A.; Mizugaki, T.; Jitsukawa, K.; Kaneda, K. Highly efficient double-carbonylation of amines to oxamides using gold nanoparticle catalysts. *Chem. Commun.* **2012**, *48*, 11733−11735.

(30) Kang, P.-L.; Shang, C.; Liu, Z.-P. Large-Scale Atomic Simulation via Machine Learning Potentials Constructed by Global Potential Energy Surface Exploration. *Acc. Chem. Res.* **2020**, *53*, 2119−2129.

(31) Huang, S.-D.; Shang, C.; Kang, P.-L.; Liu, Z.-P. Atomic structure of boron resolved using machine learning and global sampling. *Chem. Sci.* **2018**, *9*, 8644−8655.

(32) Yin, Z.; Peng, H.; Wei, X.; Zhou, H.; Gong, J.; Huai, M.; Xiao, L.; Wang, G.; Lu, J.; Zhuang, L. An alkaline polymer electrolyte CO_2 electrolyzer operated with pure water. *Energy Environ. Sci.* **2019**, *12*, 2455−2462.

(33) Kresse, G.; Furthmüller, J. Efficient iterative schemes for ab initio total-energy calculations using a plane-wave basis set. *Phys. Rev. B* **1996**, *54*, 11169−11186.

(34) Shang, C.; Zhang, X.-J.; Liu, Z.-P. Stochastic surface walking method for crystal structure and phase transition pathway prediction. *Phys. Chem. Chem. Phys.* **2014**, *16*, 17845−17856.

(35) Shang, C.; Liu, Z.-P. Constrained Broyden Minimization Combined with the Dimer Method for Locating Transition State of Complex Reactions. *J. Chem. Theory Comput.* **2010**, *6*, 1136−1144.

(36) Sankar, M.; He, Q.; Engel, R. V.; Sainna, M. A.; Logsdail, A. J.; Roldan, A.; Willock, D. J.; Agarwal, N.; Kiely, C. J.; Hutchings, G. J. Role of the Support in Gold-Containing Nanoparticles as Heterogeneous Catalysts. *Chem. Rev.* **2020**, *120*, 3890−3938.

(37) Cao, Y.; He, L. Synthesis of Carbonyl Compounds by Gold-Catalyzed Carbonylation Reactions. *Synlett* **2022**, *33*, 1003−1010.

(38) Cao, Y.; Huang, Y.; He, L. Sustainable Route Toward N-Boc Amines: $AuCl_3$ /CuI-Catalyzed N-tert-butyloxycarbonylation of Amines at Room Temperature. *ChemSusChem* **2022**, *15*, No. e202102400.

https://doi.org/10.1021/acscatal.2c05358
ACS Catal. 2023, 13, 735−743

(39) Cao, Y.; Yang, J. G.; Deng, Y.; Wang, S.; Liu, Q.; Shen, C.; Lu, W.; Che, C. M.; Chen, Y.; He, L. Amine-Responsive Disassembly of Au(I)-Cu(I) Double Salts for Oxidative Carbonylation. *Angew. Chem., Int. Ed.* **2020**, *59*, 2080−2084.
(40) Jin, L.; Weinberger, D. S.; Melaimi, M.; Moore, C. E.; Rheingold, A. L.; Bertrand, G. Trinuclear Gold Clusters Supported by Cyclic (alkyl)(amino)carbene Ligands: Mimics for Gold Heterogeneous Catalysts. *Angew. Chem., Int. Ed.* **2014**, *53*, 9059−9063.
(41) Shi, F.; Deng, Y. Polymer-Immobilized Gold Catalysts for the Efficient and Clean Syntheses of Carbamates and Symmetrical Ureas by Oxidative Carbonylation of Aniline and Its Derivatives. *J. Catal.* **2002**, *211*, 548−551.
(42) Rodriguez, J. A.; Grinter, D. C.; Liu, Z.; Palomino, R. M.; Senanayake, S. D. Ceria-based model catalysts: fundamental studies on the importance of the metal-ceria interface in CO oxidation, the water-gas shift, CO_2 hydrogenation, and methane and alcohol reforming. *Chem. Soc. Rev.* **2017**, *46*, 1824−1841.
(43) Chen, Y.; Crawford, P.; Hu, P. Recent Advances in Understanding CO Oxidation on Gold Nanoparticles Using Density Functional Theory. *Catal. Lett.* **2007**, *119*, 21−28.
(44) Yu, L.; Liu, Y.; Yang, F.; Evans, J.; Rodriguez, J. A.; Liu, P. CO Oxidation on Gold-Supported Iron Oxides: New Insights into Strong Oxide−Metal Interactions. *J. Phys. Chem. C* **2015**, *119*, 16614−16622.
(45) Shi, R.; Liao, W.; Ramirez, P. J.; Orozco, I.; Mahapatra, M.; Kang, J.; Hunt, A.; Waluyo, I.; Senanayake, S. D.; Liu, P.; Rodriguez, J. A. The Interaction of K and O_2 on Au(111): Multiple Growth Modes of Potassium Oxide and Their Catalytic Activity for CO Oxidation. *Angew. Chem.* **2022**, *134*, No. e202208666.
(46) Luo, L.; Gong, Z.; Xu, Y.; Ma, J.; Liu, H.; Xing, J.; Tang, J. Binary Au-Cu Reaction Sites Decorated ZnO for Selective Methane Oxidation to C1 Oxygenates with Nearly 100% Selectivity at Room Temperature. *J. Am. Chem. Soc.* **2022**, *144*, 740−750.
(47) Liu, J.; Qiao, B.; Song, Y.; Tang, H.; Huang, Y.; Liu, J. Highly active and sintering-resistant heteroepitaxy of Au nanoparticles on ZnO nanowires for CO oxidation. *J. Energy Chem.* **2016**, *25*, 361−370.
(48) Comotti, M.; Li, W.-C.; Spliethoff, B.; Schüth, F. Support Effect in High Activity Gold Catalysts for CO Oxidation. *J. Am. Chem. Soc.* **2006**, *128*, 917−924.
(49) Chen, S.; Abdel-Mageed, A. M.; Mochizuki, C.; Ishida, T.; Murayama, T.; Rabeah, J.; Parlinska-Wojtan, M.; Brückner, A.; Behm, R. J. Controlling the O-Vacancy Formation and Performance of Au/ZnO Catalysts in CO_2 Reduction to Methanol by the ZnO Particle Size. *ACS Catal.* **2021**, *11*, 9022−9033.
(50) Liu, X.; Liu, M. H.; Luo, Y. C.; Mou, C. Y.; Lin, S. D.; Cheng, H.; Chen, J. M.; Lee, J. F.; Lin, T. S. Strong metal-support interactions between gold nanoparticles and ZnO nanorods in CO oxidation. *J. Am. Chem. Soc.* **2012**, *134*, 10251−10258.
(51) Liu, N.; Xu, M.; Yang, Y.; Zhang, S.; Zhang, J.; Wang, W.; Zheng, L.; Hong, S.; Wei, M. $Au^{\delta-}$-O^{v}−Ti^{3+} Interfacial Site: Catalytic Active Center toward Low-Temperature Water Gas Shift Reaction. *ACS Catal.* **2019**, *9*, 2707−2717.
(52) Qian, K.; Huang, W.; Fang, J.; Lv, S.; He, B.; Jiang, Z.; Wei, S. Low-temperature CO oxidation over Au/ZnO/SiO_2 catalysts: Some mechanism insights. *J. Catal.* **2008**, *255*, 269−278.
(53) Lin, L.; Yu, Q.; Peng, M.; Li, A.; Yao, S.; Tian, S.; Liu, X.; Li, A.; Jiang, Z.; Gao, R.; Han, X.; Li, Y.-W.; Wen, X.-D.; Zhou, W.; Ma, D. Atomically Dispersed Ni/alpha-MoC Catalyst for Hydrogen Production from Methanol/Water. *J. Am. Chem. Soc.* **2021**, *143*, 309−317.
(54) Williams, W. D.; Shekhar, M.; Lee, W.-S.; Kispersky, V.; Delgass, W. N.; Ribeiro, F. H.; Kim, S. M.; Stach, E. A.; Miller, J. T.; Allard, L. F. Metallic Corner Atoms in Gold Clusters Supported on Rutile Are the Dominant Active Site during Water-Gas Shift Catalysis. *J. Am. Chem. Soc.* **2010**, *132*, 14018−14020.
(55) Yao, Y.; Chen, L.; Mao, X.; Yang, Y.; Chen, J.; Zhou, L. In Situ PM-IRRAS Study of CO Adsorption on Au Surfaces: Solving the Puzzle. *J. Phys. Chem. C* **2021**, *125*, 8606−8619.
(56) Bailie, J. E.; Abdullah, H. A.; Anderson, J. A.; Rochester, C. H.; Richardson, N. V.; Hodge, N.; Zhang, J.-G.; Burrows, A.; Kiely, C. J.; Hutchings, G. J. Hydrogenation of but-2-enal over supported Au/ZnO catalysts. *Phys. Chem. Chem. Phys.* **2001**, *3*, 4113−4121.
(57) Panayotov, D. A.; Burrows, S. P.; Yates, J. T.; Morris, J. R. Mechanistic Studies of Hydrogen Dissociation and Spillover on Au/TiO_2: IR Spectroscopy of Coadsorbed CO and H-Donated Electrons. *J. Phys. Chem. C* **2011**, *115*, 22400−22408.
(58) Phala, N. S.; Klatt, G.; Steen, E. A DFT study of hydrogen and carbon monoxide chemisorption onto small gold clusters. *Chem. Phys. Lett.* **2004**, *395*, 33−37.
(59) Pan, Y.; Wu, G.; He, Y.; Feng, J.; Li, D. Identification of the Au/ZnO interface as the specific active site for the selective oxidation of the secondary alcohol group in glycerol. *J. Catal.* **2019**, *369*, 222−232.
(60) Jobson, E.; Baiker, A.; Wokaun, A. Copper-catalyzed dehydroamination of 1-hexanol with dimethylamine: an in situ FTIR study. *J. Mol. Catal.* **1990**, *60*, 399−416.
(61) Nunes, M. H. O.; Silva, V. T. d.; Schmal, M. The effect of copper loading on the acidity of Cu/HZSM-5 catalysts: IR of ammonia and methanol for methylamines synthesis. *Appl. Catal., A* **2005**, *294*, 148−155.
(62) Jobson, E.; Baiker, A.; Wokaun, A. Adsorption of ammonia and methylamines on alumina and copper/alumina studied by dynamic fourier-transform infrared experiments. *J. Chem. Soc., Faraday Trans.* **1990**, *86*, 1131−1137.
(63) Shang, C.; Liu, Z.-P. Stochastic Surface Walking Method for Structure Prediction and Pathway Searching. *J. Chem. Theory Comput.* **2013**, *9*, 1838−1845.
(64) Huang, S.-D.; Shang, C.; Zhang, X.-J.; Liu, Z.-P. Material discovery by combining stochastic surface walking global optimization with a neural network. *Chem. Sci.* **2017**, *8*, 6327−6337.
(65) Liu, J.; Cao, X.-M.; Hu, P. Density functional theory study on the activation of molecular oxygen on a stepped gold surface in an aqueous environment: a new approach for simulating reactions in solution. *Phys. Chem. Chem. Phys.* **2014**, *16*, 4176−4185.
(66) Liu, Z.-P.; Gong, X.-Q.; Kohanoff, J.; Sanchez, C.; Hu, P. Catalytic Role of Metal Oxides in Gold-Based Catalysts: A First Principles Study of CO Oxidation on TiO_2 Supported Au. *Phys. Rev. Lett.* **2003**, *91*, No. 266102.

https://doi.org/10.1021/acscatal.2c05358
ACS Catal. 2023, 13, 735−743